Journal of ELECTRONIC MATERIALS, Vol. 42, No. 11, 2013
DOI: 10.1007/s11664-013-2737-2

Theoretical Modeling of HOT HgCdTe Barrier Detectors for the Mid-Wave Infrared Range

P. MARTYNIUK,[1,2] W. GAWRON,[1] and A. ROGALSKI[1]

1.—Institute of Applied Physics, Military University of Technology, 2 Kaliskiego St., 00-908 Warsaw, Poland. 2.—e-mail: pmartyniuk@wat.edu.pl

This paper reports on theoretical modeling of medium-wavelength infrared HgCdTe barrier infrared detector (BIRD) photoelectrical performance. BIRD HgCdTe detectors were simulated with the commercially available software APSYS. Detailed analysis of the detector performance such as dark current, photocurrent, resistance–area product, detectivity versus applied bias, operating temperature, and structural parameters (absorber doping, barrier composition) was performed to determine the optimal operating conditions. It is shown that higher operation temperature conditions achievable with commonly used thermoelectric coolers allow detectivities of $D = 9.5 \times 10^{10}$ cmHz$^{1/2}$/W and $D^* = 1.5 \times 10^{11}$ cmHz$^{1/2}$/W at $T = 200$ K to be obtained for the correct absorber doping for nB_nnn^+ and nB_npn^+, respectively. R_0A for the nB_nnn^+ detector was found to range from 200 Ω cm^2 to 0.6 Ω cm^2 at $T = 200$ K to 300 K, respectively.

Key words: HgCdTe, unipolar barrier, $nB_nn(p)$, $nB_nn(p)n^+$, Auger suppression, photoelectric gain

INTRODUCTION

Photodetectors designed for the mid-wave infrared (MWIR, 3 μm to 5 μm) region meeting the requirements for higher operation temperature (HOT) conditions are important in a variety of civilian and military applications. The key condition which must be fulfilled to design a HOT IR detector is to achieve both low dark current and high quantum efficiency (QE). In standard p–n MWIR photodiodes operating under HOT conditions, the dark current is mostly produced by the Shockley–Read–Hall (SRH) generation–recombination (GR) process, Auger, and both: band-to-band (BTB)/trap-assisted tunneling (TAT).[1–3] Unfavorable SRH and leakage current components can be suppressed by appropriate selection of barriers (wide-energy-gap materials) incorporated into the detector structure.[4] The barrier selection plays a decisive role due to the lattice constant matching of the detector's constituent layers, the barrier height in both conduction and valence bands (connected directly to the band alignment) being difficult to control from a technological viewpoint.

Currently, among barrier IR detectors (BIRDs), the leading position is occupied by devices called unipolar barrier infrared detectors (UBIRDs). $A^{III}B^{V}$ family compounds emerged to play a dominant role in the design of UBIRDs due to a nearly zero band offset in the valence band (e.g., GaSb, $InAs_{1-z}Sb_z$ cap layers, $InAs_{1-y}Sb_y$ active region, $AlAs_{1-x}Sb_x$ barrier).[5] Type II superlattices (T2SLs) of InAs/GaSb with AlGaSb/T2SL barriers (with tunneling and inherited Auger GR process suppression) and more sophisticated structures, such as the "W" (InAs/GaInSb/InAs/AlGaInSb), "M" (GaSb/InAs/GaSb/AlSb), and recently presented "N" (AlSb/GaSb/InAs) structures, have also shown promise for HOT conditions.[6–10] The success of T2SLs has resulted from the unique inherited capabilities of the new artificial material with completely different physical properties in comparison with the constituent layers and the nearly zero valence band offsets leading to advantageous BIRD band alignments that are difficult to attain in HgCdTe.[11,12]

(Received December 3, 2012; accepted August 14, 2013; published online October 1, 2013)

Although the physical properties indicate the potential superiority of T2SLs over bulk materials, we predict that, similar to the technological problems related to growth of self-organized quantum dots for quantum dot infrared photodetectors (QDIPs), the development of InAs/GaSb T2SLs will be limited by technological problems connected with the growth of uniform, sufficiently thick SLs.[13,14] In addition, short minority-carrier lifetimes (τ_{DIF}, $\tau_{GR} < 10$ ns for temperature >200 K) also impede the development of T2SL IR devices.[15]

Even though HgCdTe does not exhibit a zero valence band offset ("nested" type I heterojunction—it is impossible to design an entirely majority-carrier blocking barrier device), the BIRD (nB_nn) architecture was successfully adapted to the HgCdTe alloy, presenting technological advantages over the p–n HgCdTe homojunction [simplifying the fabrication process and circumventing the potential problems with p-type *in situ* doping in molecular beam epitaxy (MBE) growth].[16–18] On the other hand, the p-type absorber offers a better absorption coefficient and lower Auger GR, which should improve the detector performance.[19] In addition, Klem et al.[20] and Klipstein[5] reported on pB_nn InAsSb/AlAsSb detector performance, pointing out their possible capabilities when a very large barrier in the conduction band is not available, allowing for operation at zero bias.[5,20] Moving forward, an extra highly doped contact layer in the nB_nnn^+ or nB_npn^+ structure suppresses the Auger GR rate due to nonequilibrium operation (exclusion junction).[21–23] As far as nB_nnn^+ and nB_npn^+ structures are concerned, the absorber–highly doped contact layer homojunction will be decisive, and it is believed that its optimization will allow the highest performance to be obtained (especially when including TAT/BTB processes at the n–n^+ and p–n^+ homojunction).

In this paper we present the performance of BIRD MWIR HgCdTe detectors with a cutoff wavelength of $\lambda_c = 5.2$ μm at $T = 200$ K to 300 K. The temperature and bias voltage dependences of the dark current, R_0A product, and detectivity of the BIRD HgCdTe detectors with an Auger suppression mechanism are analyzed, including both TAT and BTB processes at the exclusion homojunction. Finally, the performance of a state-of-the-art thermoelectrically (TE) cooled MWIR BIRD HgCdTe detector is compared with that of $A^{III}B^{V}$ BIRD detectors.

SIMULATION PROCEDURES

Numerical calculations were performed utilizing the commercially available software APSYS. Specific equations and relations used in the device modeling are listed in the Appendix and Table I. The exclusion junction of the nB_nnn^+ and nB_npn^+ structures was modeled using both TAT and BTB mechanisms. For modeling purposes, a three-layer barrier was applied to mitigate the kinks emerging in energy band diagrams between the detector's constituent layers. In addition, a three-sublayer barrier was utilized to simulate potential issues with compositional uniformity at the interfaces. Interdiffusion was modeled by applying Gauss tail doping ($dx = 0.05$ μm). The modeled nB_nn and nB_nnn^+ structures are shown in Fig. 1a–c. A similar BIRD design was reported by Velicu and Itsuno et al.[17,23] The simulated BIRD structure consists of an n^+-type contact layer (exclusion junction) and n-type HgCdTe absorber with thickness of 5 μm doped with In ($n = 10^{14}$ cm^{-3}) with composition $x = 0.275$ for the MWIR range. After the absorber layer, an n-type HgCdTe barrier was incorporated with thickness of 0.15 μm, doped with In ($n = 2 \times 10^{15}$ cm^{-3}). As mentioned above, in our model the barrier layer was divided into three sublayers with compositional grading fitted to the cap layer and absorber, respectively (e.g., $x = 0.33$–0.6–0.275). The barrier was assumed to be thick enough to prevent electron tunneling between the top contact layer and the absorbing layer; therefore, the majority current is blocked by the barrier material under an applied bias. Finally, a 0.16-μm-thick n-type HgCdTe cap layer (doped with In to $n = 7 \times 10^{14}$ cm^{-3}) was incorporated. Ohmic contacts were implemented as simple Dirichlet boundary conditions.

The 50% cutoff wavelength was calculated to be $\lambda_c = 5.2$ μm at $T = 200$ K. The detector area equals 100 μm $\times$ 100 μm.

Table I. Parameters taken in modeling of MWIR BIRD HgCdTe detectors

	Cap	Barrier	Absorber	Contact
Donor/acceptor concentration, N_D (cm^{-3})	7×10^{14}	2×10^{15}	$10^{14} \rightarrow 5 \times 10^{16}$	5×10^{17}
Composition, x	0.33	0.33 $\rightarrow$ 0.6 $\rightarrow$ 0.275	0.275 ($\lambda_c = 5.2$ μm/$T = 200$ K)	0.275–0.4
Geometry, d (μm)	0.16	0.15	5	1
Device electrical area, A (μm^2)	100 $\times$ 100			
Background temperature, T_B, FOV	300 K, 20°			
Overlap matrix, F_1F_2	0.2			
Trap energy level, E_{Trap}	$0.25E_g$			
Trap concentration, N_{Trap} (cm^{-3})	10^{13}			
Capture cross-section, σ_n, σ_p (cm^2)	10^{-15}, 10^{-16}			
Target incident power density, Φ (W/m^2)	500			

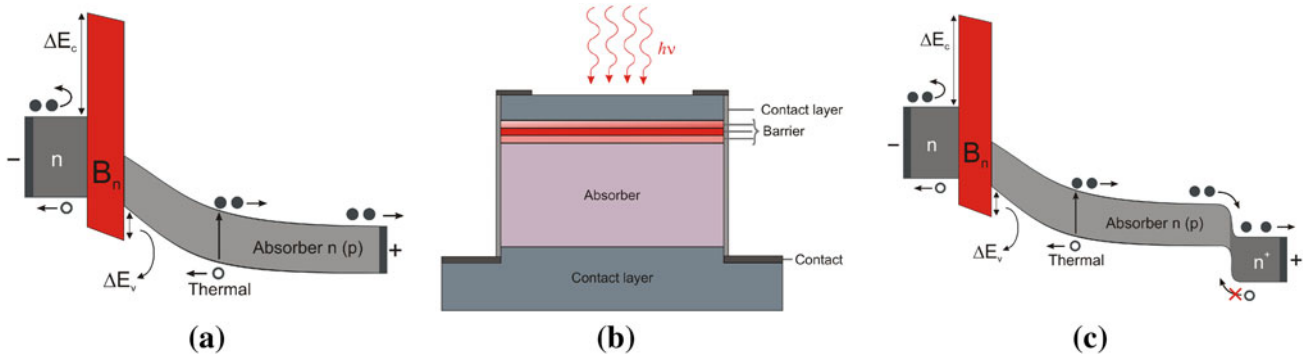

Fig. 1. Energy band diagram of the HgCdTe nB_nn photodetector under reverse-bias conditions (a); nB_nnn^+ structure (b); energy band diagram of the HgCdTe nB_nnn^+ photodetector under reverse-bias conditions (c).

The noise current was calculated using the expression including Johnson–Nyquist noise, and optical and electrical shot noises

$$i_n(V) = \sqrt{4k_BT/RA + 2qI_{DARK} + 2qI_B}, \quad (1)$$

where A is the detector area, RA is the resistance–area product, I_{DARK} and I_B are the dark current density and background induced current, respectively, and k_B is the Boltzmann constant.

The background wavelength-dependent current was calculated according to the expression

$$I_B = \frac{2\pi cq}{\lambda^4}\sin^2\left(\frac{\theta}{2}\right)\int_0^{\lambda_c}[\exp(hc/k_BT_B\lambda) - 1]^{-1}\eta(\lambda)d\lambda, \quad (2)$$

where T_B is the scene temperature, θ is the detector's field of view ($\theta = 20°$), and $T_B = 300$ K was assumed.

The QE is a function of the incident radiation wavelength. The current responsivity, R_i, was calculated according to the relation (without electro-optical gain)

$$R_i = \eta\frac{\lambda q}{hc}. \quad (3)$$

The detector's detectivity is defined by the expression

$$D^* = \frac{R_i}{i_n(V)}\sqrt{A}. \quad (4)$$

BIRD HgCdTe BAND ALIGNMENT AND SRH GR SUPPRESSION

The valence band offset (VBO) of the HgCdTe multiple-layer structure has been the subject of a longstanding controversy. Published VBO values span from 40 meV to 800 meV at liquid-helium temperature.[24,25] Becker et al. and Spicer et al. reported a VBO with the following temperature and composition dependence

$$\mathrm{VBO}(T,x) = x\left[\mathrm{VBO}_o + T\left(\frac{d\mathrm{VBO}}{dT}\right)\right], \quad (5)$$

where $\mathrm{VBO}_o = 570 \pm 60$ meV and $d\mathrm{VBO}/dT = 0.4 \pm 0.01$ meV/K.[26,27]

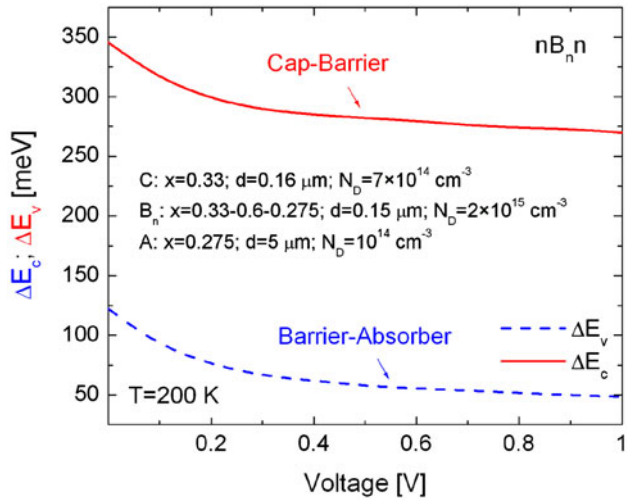

Fig. 2. ΔE_c (cap–barrier) and ΔE_v (barrier–absorber) versus applied voltage for nB_nn at $T = 200$ K.

Figure 2 presents the cap–barrier ΔE_c and barrier–absorber ΔE_v versus applied voltage. As far as reverse-biased BIRD nB_nn and nB_np HgCdTe detectors are concerned, the most crucial of these is the ΔE_c emerging at the cap–barrier interface (desirable majority-carrier blocking from the cap layer) and the ΔE_v at the barrier–absorber interface (unfavorable minority-carrier blocking). Both ΔE_c and ΔE_v depend directly on the applied voltage, and it is clear that there is a trade-off in applied voltage between ΔE_c and ΔE_v (e.g., for barrier–absorber interface $\Delta E_v \approx 120$–50 meV and cap–barrier interface $\Delta E_c \approx 350$–275 meV; $V = 0$–1 V for nB_nn). Above $V = 0.4$ V, ΔE_c and ΔE_v reach almost constant values of 270 meV and 50 meV, respectively,

leading to the dark and photocurrent increasing slightly (nB_nn). The ΔE_c and ΔE_v values of nB_np (absorber $p = 10^{14}$ cm^{-3}) structures are slightly higher in comparison with those exhibited by the nB_nn (absorber $n = 10^{14}$ cm^{-3}) photodetector.

The doping and composition of the barrier also influence ΔE_c and ΔE_v. As the barrier's composition increases, ΔE_c and ΔE_v rise, but ΔE_c changes more rapidly in comparison with ΔE_v, which influences the detector dark and photocurrents. Increase of the barrier doping reduces the cap–barrier ΔE_c and raises ΔE_v. The simulated ΔE_c and ΔE_v values versus barrier composition and doping for the nB_nn structure are presented in Fig. 3.

Bandgap engineering reduces the SRH GR rate in the depletion region and reduces the net current by controlling single carrier flow (nB_nn—assuming zero valence band offset), which is blocked by a wide-gap barrier region [$J_{DARK} \sim \exp(-E_g/2k_BT)$]. Taking this into consideration, $|R_{SRH}|$ will be reduced when the depletion region is excluded from the absorber layer. This condition will be met if both barrier and absorber layer are n (p)-type doped. If either the barrier or absorber layer has the opposite doping type, a wider depletion region develops, which increases the $|R_{SRH}|$ GR rate, potentially decreasing the detector performance. Figure 4 presents the $|R_{SRH}|$ rate calculated for the p–n junction and nB_nn(p) structures at $T = 200$ K, $V = 0.3$ V, and barrier $x = 0.6$. The incorporation of a wide-gap barrier reduces $|R_{SRH}|$ by five orders of magnitude in comparison with the p–n ($x = 0.275$) junction. The composition's influence on the $|R_{SRH}|$ rate in the "middle" of the barrier is presented in Fig. 5. $|R_{SRH}|$ for the nB_np structure is slightly lower in comparison with nB_nn (the depletion region moves to the absorber region), while at $T = 300$ K both $|R_{SRH}|$ reach the same values. On increasing the reverse voltage to $V = 1$ V ($T = 200$ K), for a barrier with $x < 0.5$ the opposite $|R_{SRH}|$ dependence is observed [$|R_{SRH}|(nB_np) > |R_{SRH}|(nB_nn)$]. In the absorber region, $|R_{SRH}|(nB_np) > |R_{SRH}|(nB_nn)$. Increasing the x value of the barrier from 0.46 to 0.62 reduces J_{DARK} by nearly one order of magnitude for both nB_nn(p) structures.

BIRD HgCdTe CONTACT ARRANGEMENT AND SRH GR SUPPRESSION

The intrinsic Auger process characteristically dominates at elevated temperatures due to the fact that the low-level-doped absorbers become intrinsic, which increases the carrier concentration above the

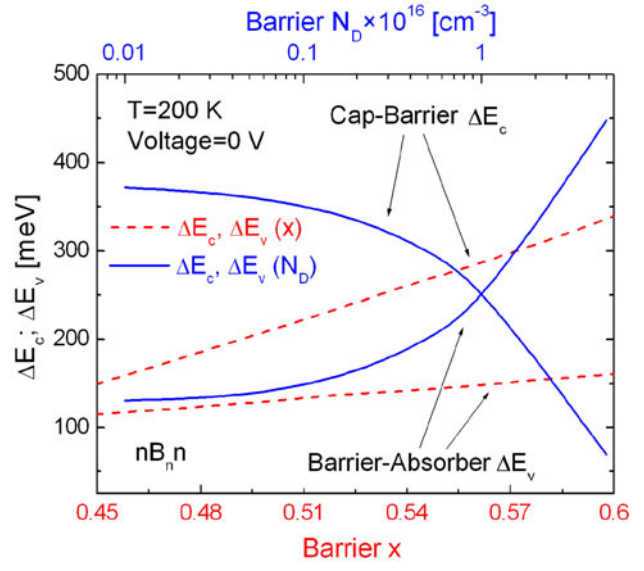

Fig. 3. ΔE_c (cap–barrier) and ΔE_v (barrier–absorber) versus barrier composition x and doping for unbiased nB_nn structure and $T = 200$ K.

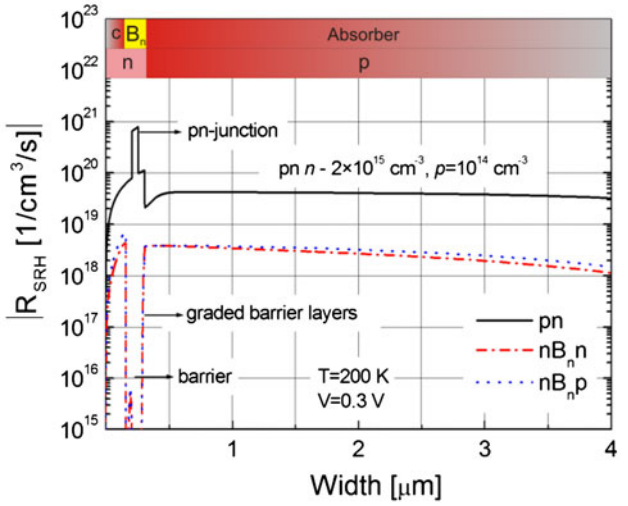

Fig. 4. $|R_{SRH}|$ for p–n and BIRD nB_nn(p) structures at $T = 200$ K and $V = 0.3$ V.

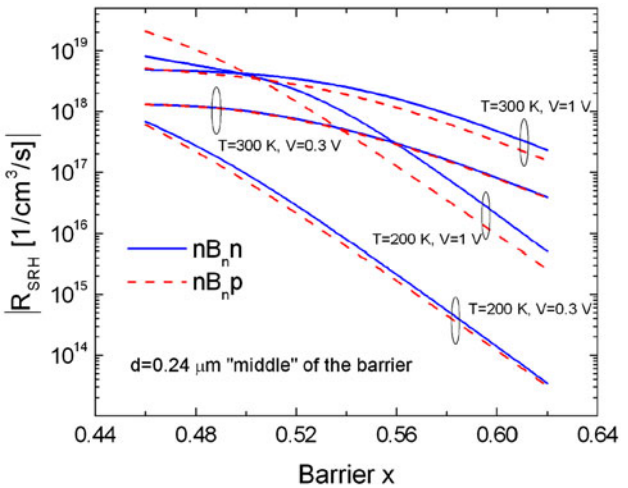

Fig. 5. $|R_{SRH}|$ for BIRD nB_nn(p) structures versus barrier x at $T = 200$ K/300 K and $V = 0.3$ V/1 V.

doping level. Proper contact layer arrangement (n^+/N^+) by incorporation of either high doping or wide-gap material suppresses Auger GR by reducing carrier densities below the thermal equilibrium. The intrinsic concentration for the simulated structures was estimated to be at the level $n_i = 5 \times 10^{14}$ cm^3 at $T = 200$ K. The Auger GR rates for different HgCdTe BIRD architectures are presented in Figs. 6 and 7.

Incorporation of the n^+ exclusion contact reduces the net $|R_{AUG}|$ by two orders of magnitude (nB_npn^+), which leads to reduction of J_{DARK} by nearly three orders of magnitude. Increasing the composition of the contact layer to $x = 0.4$ (incorporation of the N^+ contact layer) increases the R_0A product nearly twofold.

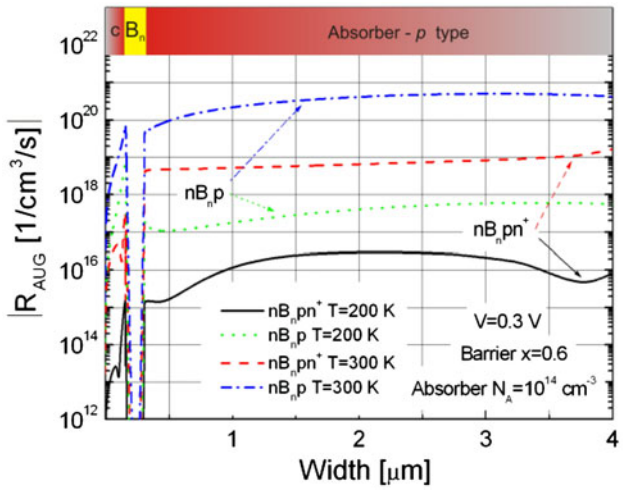

Fig. 6. $|R_{AUG}|$ for BIRD nB_np and nB_npn^+ structures at $T = 200$ K and $V = 0.3$ V.

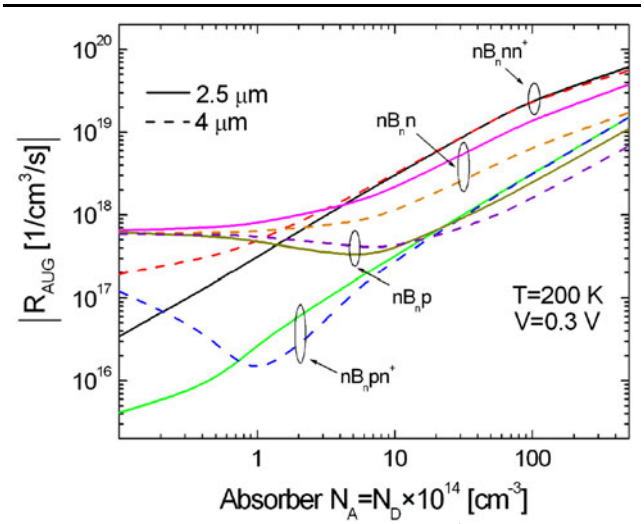

Fig. 7. $|R_{AUG}|$ for BIRD $nB_n(p)$ and $nB_n(p)n^+$ structures versus absorber doping x at $T = 200$ K and $V = 0.3$ V.

BIRD HgCdTe DARK CURRENT SIMULATION

Figures 8 and 9 depict the calculated dark current densities versus reverse bias for the nB_nn/nB_nnn^+ and nB_np nB_npn^+ detectors at $T = 200$ K (an operating temperature obtainable using TE cooling). The simulations performed include the radiative (RAD), SRH, and Auger GR mechanisms. The influence of both the electron and hole barriers is clearly evident in the J–V characteristics, where the turn-on voltage (i.e., the voltage required to align the ΔE_c and ΔE_v barriers) was assumed to be $V = 0.3$ V for the nB_nn ($V > 0.3$ V for nB_np) structure, while $V = 0.1$ V was estimated for $nB_n(p)n^+$

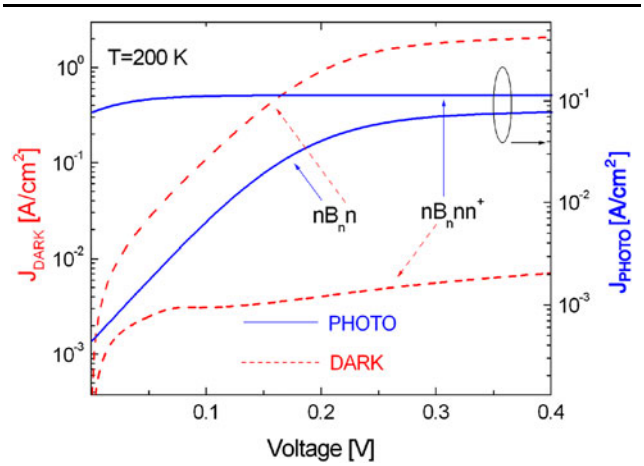

Fig. 8. J_{DARK}/J_{PHOTO} versus voltage for BIRD nB_nn and nB_nnn^+ at $T = 200$ K.

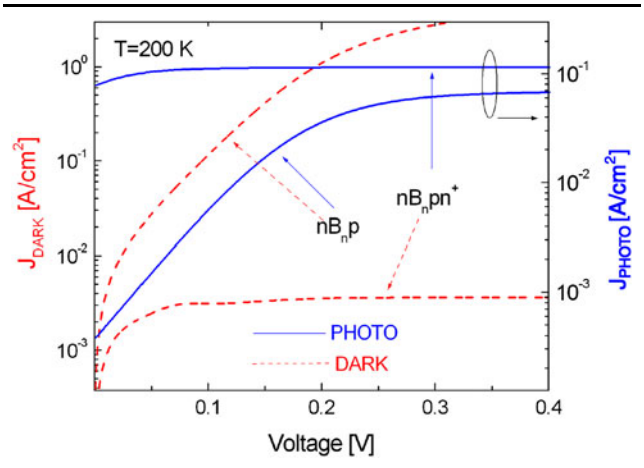

Fig. 9. J_{DARK}/J_{PHOTO} versus voltage for BIRD nB_np and nB_npn^+ at $T = 200$ K.

architectures (Fig. 2). J_{DARK} for the reverse-biased nB_np detector is higher in comparison with the nB_nn structure at $T = 200$ K due to the greater influence of the $|R_{SRH}|$ rate from the wider depletion region and the hole injection by the ohmic contact to the absorber area.

Incorporation of the hole barrier (n^+) allows a reduction of the dark current by more than two orders of magnitude depending on the operating temperature for both $nB_nn(p)n^+$ detectors. Photoconductive behavior is observed for the n-type absorber structure, where a slight increase of J_{DARK} is evident versus the applied bias (for the detector structure consisting of four n-type-doped layers). In addition, the Auger GR suppression is clearly visible around $V = 0.1$ V, where negative differential resistance (NDR) is observable. Since the p-type absorber exhibits lower Auger GR rates (nB_npn^+), J_{DARK} is reduced in comparison with the structure with the n-type absorber.

The photocurrent density follows the J_{DARK} voltage dependence, exhibiting similar turn-on voltages visible as characteristic kinks in the J–V curves.

The choice of the composition and doping of the barrier plays a crucial role in the design of BIRD HgCdTe detectors (Fig. 3). Both ΔE_c and ΔE_v increase with composition, but ΔE_c rises more rapidly in comparison with ΔE_v. Figure 10 presents nB_nn J_{DARK}/J_{PHOTO} versus barrier composition for selected voltages. The optimal barrier x strictly depends on the applied voltage. Once the detector is reverse biased above the turn-on voltage, J_{DARK} retains a constant value for $x > 0.54$, while below this value the dark current density increases nearly twofold. The same trend is visible for J_{PHOTO}. The influence of the barrier x value on J_{DARK}/J_{PHOTO} for the nB_nnn^+ detector is presented in Fig. 11. The simulations were performed including RAD, SRH, and Auger GR processes. Increase of the barrier x value from $x = 0.46$ to 0.62 decreases J_{DARK} by nearly three orders of magnitude depending on the applied voltage, while J_{PHOTO} decreases by nearly one order of magnitude and exhibits a constant value for $x > 0.54$ (0.1 A/cm^2) (Fig. 11).

The doping of the absorber also plays a crucial role and must be optimized for assumed voltages. When the doping of the nB_nnn^+ absorber increases from 10^{13} cm^{-3} to 5×10^{16} cm^{-3}, the photocurrent decreases, lowering the responsivity R_i from 2 A/W to 0.2 A/W and the QE from 50% to 5% (Fig. 12 for RAD, SRH, and AUG). Due to the inclusion of the BTB and TAT mechanism at the absorber–highly doped n^+ contact layer (n–n^+), photoelectrical gain ($g = 1.5$ assuming $\eta = 50\%$) emerges, increasing R_i nearly twofold for voltages $V > 0.1$ V. The g is evident for absorber doping $N_D < 10^{16}$ cm^{-3}. In addition, increase of the absorber doping weakens the n–n^+ homojunction properties related to the Auger GR suppression. As presented in Fig. 13, the BTB/

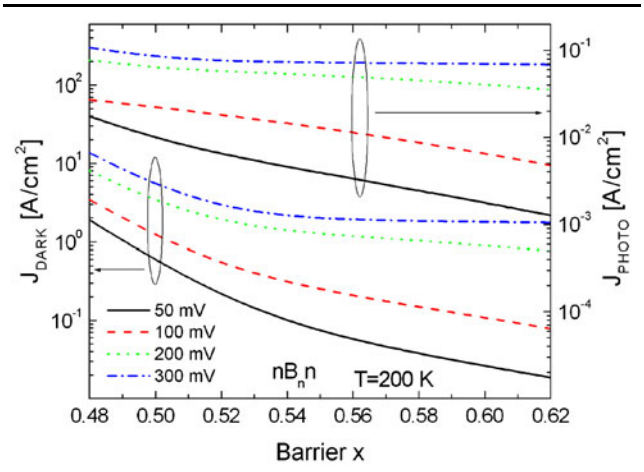

Fig. 10. J_{DARK}/J_{PHOTO} versus barrier composition for BIRD nB_nn detector at $T = 200$ K.

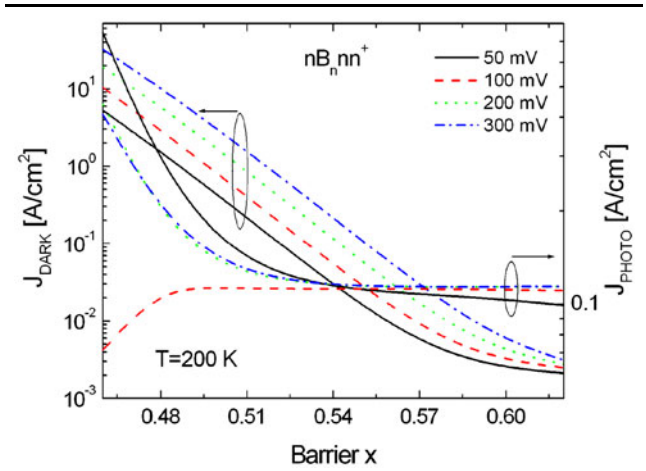

Fig. 11. J_{DARK}/J_{PHOTO} versus barrier composition for BIRD nB_nnn^+ detector at $T = 200$ K.

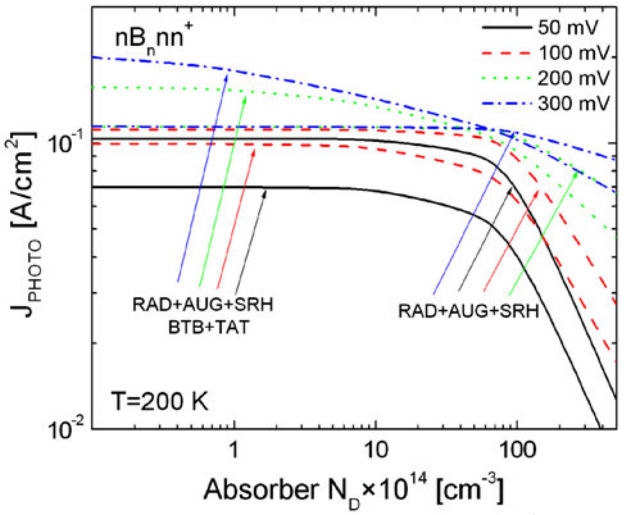

Fig. 12. J_{PHOTO} versus absorber doping for BIRD nB_nnn^+ detector. $T = 200$ K.

TAT mechanism at the n–n^+ junction does not influence J_{DARK}. Once the detector is in the illuminated condition, the quasi-Fermi levels move, increasing the probability of both tunneling mechanisms. Much higher gain is observed for the nB_npn^+ structure, where J_{PHOTO} increases fourfold, yielding R_i = 8 A/W and g = 3 (assuming η = 50%). We believe that this gain arises from the difference between electron and hole transport caused by both barriers.

BIRD HgCdTe DETECTIVITY SIMULATION

The direct dependence of ΔE_c and ΔE_v on the barrier composition and voltage is responsible for both the dark and photocurrent characteristics, which influences D^*. As shown in Figs. 14 and 15, the optimal composition to attain the highest D^* for both nB_nn and nB_np strictly increases with applied voltage (e.g., for V = 0.2 one has x = 0.54, while for V = 0.3 V one has x = 0.575). The simulated structures reach $D^* = 1.8 \times 10^9$ cmHz$^{1/2}$/W (nB_nn) and 1.2×10^9 cmHz$^{1/2}$/W (nB_np) for V = 0.3 V and T = 200 K, comparable to results presented by Velicu et al.[17] For $nB_nn(p)n^+$ structures, the detectivity rises with the barrier composition, exhibiting values nearly two orders of magnitude higher ($D^* = 7 \times 10^{10}$ cmHz$^{1/2}$/W for V = 0.1 V) compared with the $nB_nn(p)$ detectors, being comparable to the results presented by Itsuno et al.[23] As mentioned, the highest D^* is obtained for V = 0.1 V, which was assumed to be the turn-on voltage limit for J_{DARK} [$nB_nn(p)n^+$ structures].

Figures 16 and 17 present D^* versus absorber doping for selected voltages, simulated with and

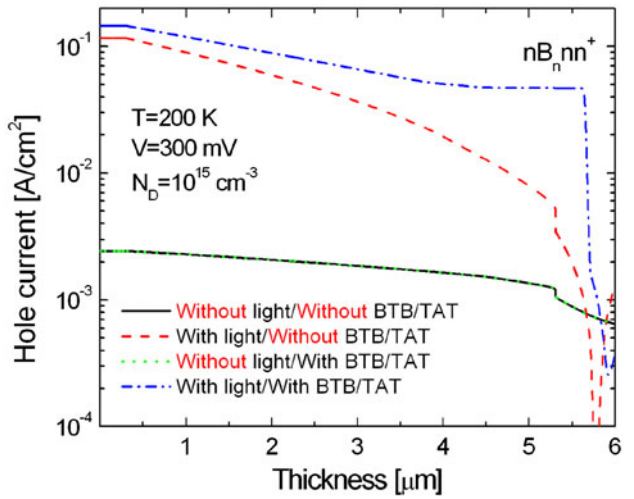

Fig. 13. Hole current density versus detector width for nB_nnn^+ structure for illuminated and BTB/TAT conditions. T = 200 K, V = 0.3 V, $N_D = 10^{15}$ cm^{-3}.

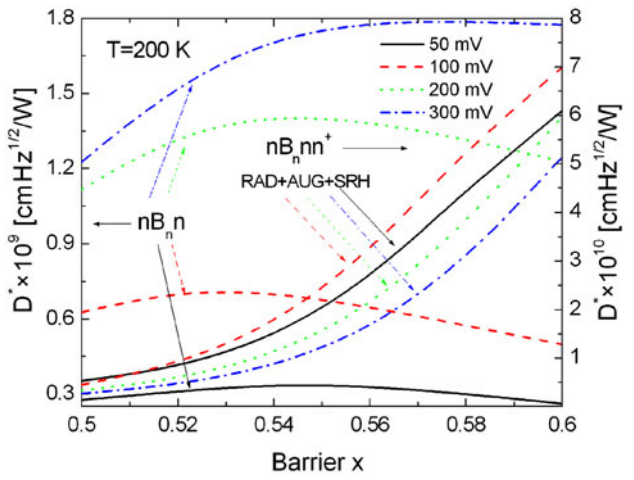

Fig. 14. D^* for BIRD nB_nn and nB_nnn^+ HgCdTe versus barrier composition for selected voltages. T = 200 K.

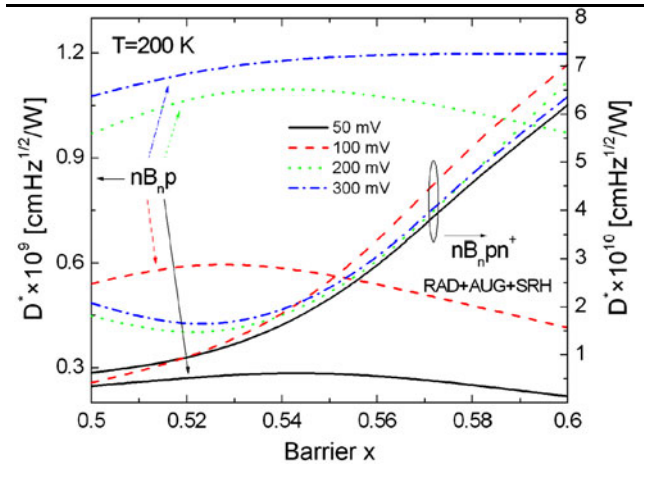

Fig. 15. D^* for BIRD nB_np and nB_npn^+ HgCdTe versus barrier composition for selected voltages. T = 200 K.

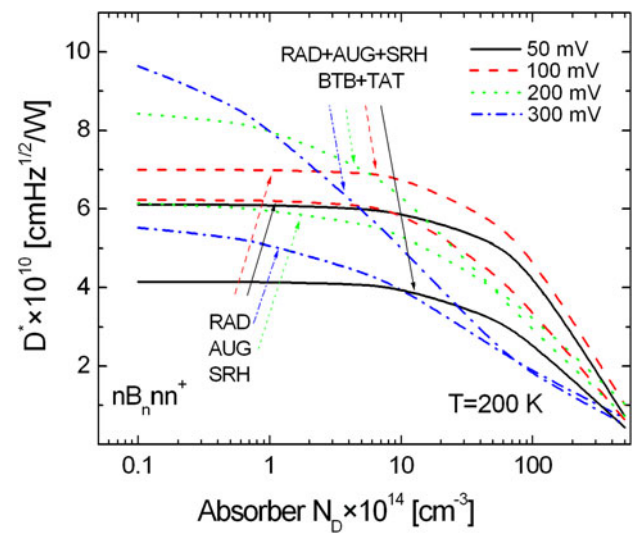

Fig. 16. D^* for BIRD nB_nnn^+ HgCdTe versus absorber doping for selected voltages. T = 200 K.

without the BTB/TAT mechanism at the n–n^+ and p–n^+ junction.

The presented results indicate that correct optimization of both junctions allows D^* to be increased to the level of 9.5×10^{10} cmHz$^{1/2}$/W and 1.5×10^{11} cmHz$^{1/2}$/W for the nB$_n$nn$^+$ and nB$_n$pn$^+$ structures, respectively. It must be noted that optimal doping to attain the highest D^* for $V > 0.1$ V in the n-type absorber structure should be $N_D < n_i$ ($n_i = 5 \times 10^{14}$ cm^{-3}), while for the p-type absorbers $N_A \approx n_i$.

COMPARISON OF IR TECHNOLOGIES

Figure 18 shows the simulated J_{DARK} versus the operating temperature for the MWIR BIRD HgCdTe structures ($\lambda_c = 5.2$ μm, $T = 200$ K) in comparison with experimental dark current densities for the following detectors: InAs/GaSb with AlGaSb barrier T2SL nB$_p$n ($\lambda_c = 5.4$ μm, $T = 230$ K), InAsSb with AlAsSb barrier ($\lambda_c = 5.05$ μm, $T = 200$ K), and the HOT HgCdTe nB$_n$n detector ($x = 0.3$).[17,28–30] The particular significance of the incorporation of the extra barrier for carriers (n^+) in the BIRD nB$_n$nn$^+$ structures versus the single barrier (potential majority-carrier blocking) is clearly evident from the J_{DARK} decrease from 3 A/cm^2 to 7×10^{-3} A/cm^2 and 40 A/cm^2 to 3 A/cm^2 for $T = 200$ K and $T = 300$ K, respectively. Proper contact layer arrangement increases the operating temperature by close to 75 K for $V = 0.4$ V. The absorber's p-type doping (assuming the same level of doping $N_D = N_A = 10^{14}$ cm^{-3}) leads to a further decrease of J_{DARK} to the level of 4×10^{-3} A/cm^2 and 2 A/cm^2 for $T = 200$ K and $T = 300$ K, respectively. In comparison with other BIRD detectors operating close to 5 μm and $V = 0.4$ V, it is evident that the HgCdTe barrier structures reach comparable values of dark current density.

In addition, having taken the difference in the absorber's composition into consideration, we may assume that the presented results coincide with these published by Velicu et al.[17,28] Comparing the nB$_n$n and nB$_n$p detectors, it is clearly evident that the SRH contribution is totally suppressed for the n-type absorber structures (diffusion limited), while the p-type absorber architecture exhibits a two-slope behavior with a crossover temperature estimated at the level of $T_c = 227$ K. Both nB$_n$nn$^+$ and nB$_n$pn$^+$ detectors are diffusion limited (one-slope behavior).

Figure 19 compares the R_0A ($k_BT/q/J_s$; $V = 1$ mV for BIRD structures) product for nB$_n$n, nB$_n$nn$^+$, and nB$_n$nN$^+$ (the N^+ layer, similarly to the barrier, consists of two sublayers—the very first one fitted with a graded composition to the absorber and the second with $x = 0.4$) versus the values given by

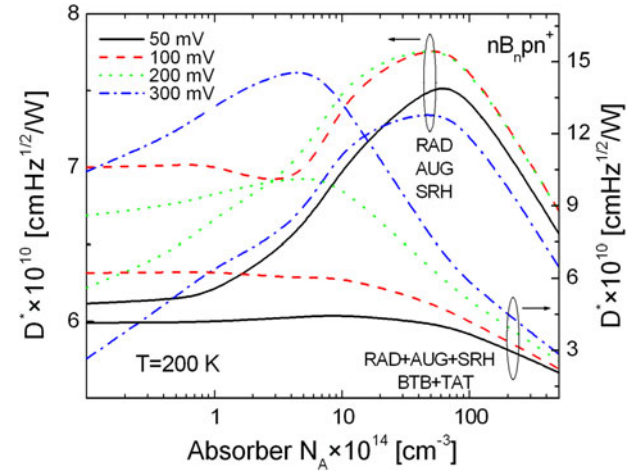

Fig. 17. D^* for BIRD nB$_n$pp$^+$ HgCdTe versus absorber doping for selected voltages. $T = 200$ K.

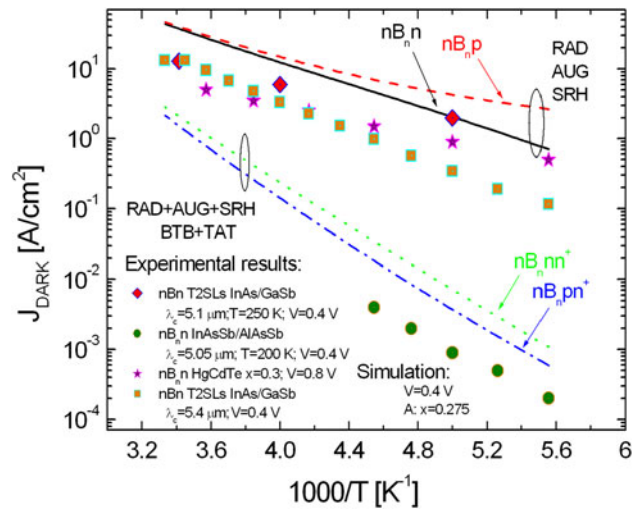

Fig. 18. J_{DARK} for MWIR BIRD structures: HgCdTe nB$_n$n detector, InAs/GaSb/B-AlGaSb T2SL nB$_p$n detector, and InAsSb/AlAsSb nB$_n$n detector.

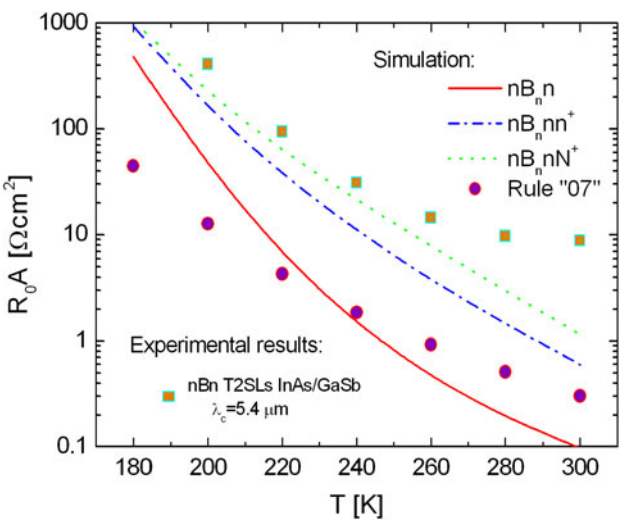

Fig. 19. R_0A product for MWIR BIRD structures: HgCdTe nB$_n$n detector, InAs/GaSb/B-AlGaSb T2SL nB$_p$n detector.

"Rule 07," being a simple means to compare mercury cadmium telluride (MCT) IR detectors.[31] It is clearly evident that the values calculated for nB_nn surpass Rule 07 below $T = 240$ K, while the above-presented results lie below the R_0A product values reported for HgCdTe photodiodes. This could be connected with the trap level in the absorber region with a density of $N_T = 10^{13}$ cm^{-3}. Proper contact arrangement increases R_0A above the values predicted by Rule 07 by nearly four times for $T = 300$ K. It is worth noting that the measured R_0A values for the T2SL InAs/GaSb nBn detector surpass the HgCdTe detectors, especially for $T > 260$ K, which could be attributed to the inherited T2SL Auger GR suppression.

CONCLUSIONS

We theoretically estimated the performance of BIRD $nB_nn(p)$ and $nB_nn(p)n^+$ SRH and Auger-GR-suppressed detectors as a function of operating conditions and structural parameters. The maximum R_0A product of the nB_nnn^+ (N^+) BIRD detector with a 5.2 μm cutoff wavelength ranges from 0.6 Ω cm^2 to 1 Ω cm^2 at $T = 300$ K, while the maximum detectivity was estimated to be 1.5×10^{11} cmHz$^{1/2}$/W (nB_npn^+ with absorber doping $N_A = 10^{14}$ cm^{-3}) at $T = 200$ K assuming absorber thickness of $d = 5$ μm and $V = 0.3$ V. Inherited barriers in both conduction and valence bands were analyzed in detail, pointing to the optimal operating conditions as far as bias and doping are concerned for the $nB_nn(p)$ structure. The turn-on voltage was estimated to be $V = 0.1$ V and $V = 0.3$ V for the $nB_nn(p)n^+$ and nB_nn structures, respectively.

Although it is unfeasible to attain the desired band alignment in the valence band, the BIRD HgCdTe structures demonstrate a performance which underlines the significance of the incorporation of the barriers into the detector architecture. Similarly, proper contact layer arrangement and its optimization increases the detector performance for both nB_nnn^+ and nB_npn^+ architectures. Even though the analyzed BIRD and nB_nnn^+ structures allow one to circumvent the requirements for p-type doping, their performance is nearly two times lower in comparison with the nB_npn^+ structure. The doping and composition of the barrier and contact layers should be perceived as the most important parameters in optimization of the BIRD HgCdTe structure. Proper choice of doping and composition leads to either the build-up or lowering of the barriers in both the conduction and valence bands. It is shown that an increase of the operating temperature by nearly 75 K (bias $V = 0.4$ V) could be achieved by the additional incorporation of the n^+/N^+ barrier into the UBIRD structure. The extra barrier leads to suppression of the dark current by nearly three orders of magnitude for $T = 200$ K.

BIRD nB_nn detectors could surpass the performance set by Rule 07 only for $T < 240$ K, where the SRH GR process limits the detector dark current characteristics.

ACKNOWLEDGEMENTS

This work has been carried out under the financial support of project PBS1/B5/2/2012.

APPENDIX

The BIRD HgCdTe detectors were simulated using the following material parameters:[32]

Band-gap energy

$$E_g(x,T) = -0.302 + 1.93x - 0.81x^2 + 0.832x^3 + 5.35 \times 10^{-4}T(1-2x) \quad \text{(A.1)}$$

Electron affinity

$$\gamma = 4.23 - 0.813\left(E_g(x,T) - 0.083\right) \quad \text{(A.2)}$$

Effective masses of carriers

$$m_e^* = 8.035 \times 10^{-2} E_g(x,T) m_0 \quad \text{(A.3)}$$

$$m_h^* = 0.55 m_0 \quad \text{(A.4)}$$

Dielectric constant

$$\varepsilon = 20.5 - 15.5x + 5.7x^2 \quad \text{(A.5)}$$

Radiative recombination rate

$$R_{RAD} = 5.8 \times 10^{-19} \varepsilon^{0.5} \left(m_e^* + m_h^*\right)^{-1.5} \left(1 + m_e^{*-1} + m_h^{*-1}\right) \times \left(\frac{300}{T}\right)^{1.5} \times \left(E_g^2 + 3k_B T E_g + 3.75 k_B^2 T^2\right) \quad \text{(A.1)}$$

Auger recombination coefficients C_n and C_p

$$C_n = \left[2n_i^2 \frac{3.8\times10^{-18}\varepsilon^2\left(1+2\frac{m_e^*}{m_h^*}\right)\left(1+\frac{m_e^*}{m_h^*}\right)^{0.5}}{m_e^*|F_1F_2|^2\left(\frac{k_BT}{E_g}\right)^{1.5}} \times \exp\left(\frac{1+2\frac{m_e^*}{m_h^*}E_g}{1+\frac{m_e^*}{m_h^*}k_BT}\right)\right]^{-1},$$

$$C_n = \left[2n_i^2 \frac{3.8\times10^{-18}\varepsilon^2\left(1+2\frac{m_e^*}{m_h^*}\right)\left(1+\frac{m_e^*}{m_h^*}\right)^{0.5}}{m_e^*|F_1F_2|^2\left(\frac{k_BT}{E_g}\right)^{1.5}} \times \exp\left(\frac{1+2\frac{m_e^*}{m_h^*}E_g}{1+\frac{m_e^*}{m_h^*}k_BT}\right)\right]^{-1} \quad (A.7)$$

$$C_p = \left(\frac{6\left(1+\frac{5E_g}{4k_BT}\right)}{1-\frac{3E}{2k_BT}}\right)^{-1} C_n \quad (A.8)$$

SRH and TAT recombination coefficients

$$R_{SRH} = \frac{np-n_i^2}{\tau_p(n+n_1)+\tau_n(p+p_1)},$$
$$R_{TRAP} = \frac{np-n_i^2}{\frac{\tau_p}{\Gamma_p+1}(n+n_1)+\frac{\tau_n}{\Gamma_n+1}(p+p_1)} \quad (A.9)$$

Mobility field dependence

$$\mu_{n/p} = \frac{\mu_{on/p}}{\left(1+\left(\frac{\mu_{on/p}}{V_{sn/p}}\right)^{B_{n/p}}\right)^{1/B_{n/p}}} \quad V_{sn/p} = 10^5\sqrt{\frac{300}{T}} \quad (A.10)$$

Absorption coefficient
For $\lambda > \lambda_c$:

$$\alpha = \alpha_o\left(\frac{\alpha_g}{\alpha_o}\right)^{\xi}, \quad (A.11)$$

$$\xi = \frac{1.24/\lambda_c - e_o}{e_g - e_o}; \quad (A.12)$$

For $\lambda \le \lambda_c$

$$\alpha = \alpha_g \exp\left(\sqrt{B(1.24/\lambda_c - e_g)}\right), \quad (A.13)$$

$$e_g = -0.295 + 1.87x - 0.28x^2 + (6 - 14x + 3x^2) \times 10^{-4}T + 0.35x^4, \quad (A.14)$$

$$\alpha_g = -65 + 1.883T + (8694 - 10.314T)x, \quad (A.15)$$

$$\alpha_o = \exp(-18.5 + 45.68x), \quad (A.16)$$

$$e_o = -0.355 + 1.77x, \quad (A.17)$$

$$B = \sqrt{-1 + 0.083T + (21 - 0.13T)x} \quad (A.18)$$

REFERENCES

1. A. Rogalski, *Infrared Detectors*, 2nd ed. (Boca Raton, FL: CRC Press, 2011).
2. K. Jóźwikowski, M. Kopytko, J. Piotrowski, A. Jóźwikowska, Z. Orman, and A. Rogalski, *Solid-State Electron.* 63, 8 (2011).
3. K. Jóźwikowski, A. Jóźwikowska, M. Kopytko, A. Rogalski, and L.R. Jaroszewicz, *Infrared Phys. Technol.* 55, 98 (2012).
4. S. Maimon and G. Wicks, *Appl. Phys. Lett.* 89, 151109-1 (2006).
5. P. Klipstein, *Proc. SPIE.* 6940, 69402U-1 (2008).
6. D.Z.-Y. Ting, A. Soibel, L. Höglund, J. Nguyen, C.J. Hill, A. Khoshakhlagh, and S.D. Gunapala, *Semiconductors and Semimetals*, vol. 84, ed. S.D. Gunapala, D.R. Rhiger, and C. Jagadish (Amsterdam: Elsevier, 2011), pp. 1–57.
7. D.Z. Ting, C.J. Hill, A. Soibel, J. Nguyen, S. Keo, M.C. Lee, J.M. Mumolo, J.K. Liu, and S.D. Gunapala, *Proc. SPIE.* 7660, 76601R (2010).
8. E.H. Aifer, J.G. Tischler, J.H. Warner, I. Vurgaftman, J.C. Kim, J.R. Meyer, B.R. Bennett, and L.J. Whitman, *Proc. SPIE.* 5732, 259 (2005).
9. B.M. Nguyen, D. Hoffman, P.Y. Delaunay, and M. Razeghi, *Appl. Phys. Lett.* 91, 163511 (2007).
10. O. Salihoglu, A. Muti, K. Kutluer, T. Tansel, and R. Turan, *Appl. Phys. Lett.* 101, 073505 (2012).
11. A. Rogalski and P. Martyniuk, *Infrared Phys. Technol.* 48, 39 (2006).
12. J.B. Rodriguez, E. Plis, G. Bishop, Y.D. Sharma, H. Kim, L.R. Dawson, and S. Krishna, *Appl. Phys. Lett.* 91, 043514-1 (2007).
13. P. Martyniuk and A. Rogalski, *Proc. SPIE* 6940, 694004 (2008).
14. P. Martyniuk and A. Rogalski, *Bull. Pol. Acad. Tech. Sci.* 57, 103 (2009).
15. J. Wróbel, P. Martyniuk, E. Plis, P. Madejczyk, W. Gawron, S. Krishna, and A. Rogalski, *Proc. SPIE.* 8353, 8353-16 (2012).
16. A.M. Itsuno, J.D. Philips, and S. Velicu, *J. Electron. Mater.* 40, 9 (2011).
17. S. Velicu, J. Zhao, M. Morley, A.M. Itsuno, and J.D. Philips, *Proc. SPIE.* 8268, 82682X (2012).
18. P. Martyniuk and A. Rogalski, *Solid-State Electron.* 80, 96 (2013).
19. J.W. Garland and Ch. Grein, *Extended Abstracts, The 2012 Workshop on the Physics and Chemistry of II–VI Materials*, Seattle (2012).
20. J.F. Klem, J.K. Kim, M.J. Cich, S.D. Hawkins, T.R. Fortune, and J.L. Rienstra, *Proc. SPIE.* 7608, 76081P (2010).
21. P.Y. Emelie, J.D. Philips, S. Velicu, and C.H. Grein, *J. Electron. Mater.* 36, 8 (2007).
22. A.M. Itsuno, J.D. Philips, and S. Velicu, *IEEE Trans. Electron Devices* 58, 2 (2011).
23. A.M. Itsuno, J.D. Philips, and S. Velicu, *J. Electron. Mater.* 40, 9 (2012).
24. Y. Guldner, Y.G. Bastard, J.P. Vieren, and M. Voos, *Phys. Rev. Lett.* 51, 907 (1983).
25. Z. Yang, Z. Yu, and Y. Lansari, et al., *Phys. Rev. B* 49, 8096 (1994).

26. M. Schultz, U. Merkt, and A. Sonntag, et al., *Phys. Rev. B* 57, 14772 (1998).
27. C.K. Shih and W.E. Spicer, *Phys. Rev. Lett.* 58, 2594 (1987).
28. A.M. Itsuno, J.D. Phillips, and S. Velicu, *Appl. Phys. Lett.* 100, 161102 (2012).
29. P. Martyniuk, J. Wrobel, E. Plis, P. Madejczyk, A. Kowalewski, W. Gawron, S. Krishna, and A. Rogalski, *Semicond. Sci. Technol.* 27, 055002 (2012).
30. A.I. D'souza, E. Robinson, A.C. Ionescu, D. Okerlund, T.J. De Lyon, H. Sharifi, M. Roebuck, D. Yap, R.D. Rajavel, N. Dhar, P.S. Wijewarnasuriya, and C. Grein, *J. Electron. Mater.* 41, 10 (2012).
31. W.E. Tennant, D. Lee, M. Zandian, E. PiQuette, and M. Carmody, *J. Electron. Mater.* 37, 9 (2008).
32. APSYS Macro/User's Manual ver. 2011 (Burnaby: Crosslight Software, Inc., 2011).